

STRUCTURAL AND TEXTURAL CHANGES OF CVD-SiC TO INDENTATION, HIGH TEMPERATURE CREEP AND IRRADIATION

G. CHOLLON^{1*}, J.M. VALLEROT¹, D. HELARY^{1,2} and S. JOUANNIGOT¹

¹ Laboratoire des Composites Thermostructuraux (LCTS), UMR 5801 (CNRS-SNECMA-CEA-UB1), Université Bordeaux 1, 3, allée de La Boétie, 33600, Pessac, France

² Commissariat à l'Energie Atomique, CEA/DEN/VRH/DTEC/STCF, BP 111, 26702, Pierrelatte, France

ABSTRACT

The structure and microtexture of different SiC based CVD coatings have been studied by RMS, in their as-processed state and after high temperature annealing, creep, indentation and irradiation. Both annealing and creep resulted in the same degree of SiC crystal growth and decrease of stacking faults. A slight influence of stress was however observed on the structure and texture of the co-deposited free-carbon, likely as a consequence of the intergranular creep mechanism. Room temperature indentation induces substantial structural disorders (dislocations, stacking faults, small grains) near the contact and more extended damages due to dislocation slip parallel to the compact Si-C planes. These structural changes were found to depend on the single crystal orientation and therefore, on the texture of

* Corresponding author: Tel.: +33 5 56 84 47 27, Fax: +33 5 56 84 12 25, E-mail address: chollon@lcts.u-bordeaux1.fr

polycrystalline SiC. Room temperature proton irradiation produced only small amounts of disorders. The specific alterations of the Raman features were explained using a phonon confinement model. This approach supports the existence of very low scale defects, likely as punctual defects.

Key Words: Defects (B.); Creep (C.), Plasticity (C.); SiC (D.); Raman Spectroscopy

1 INTRODUCTION

Chemical vapour deposited silicon carbide (CVD-SiC) is an excellent candidate for high temperature structural applications, because of its exceptional range of mechanical and thermal properties. CVD-SiC is deposited for instance on tungsten or carbon monofilament cores, for the reinforcement of metal matrix composites.¹⁻³ The filaments obtained display outstanding mechanical properties such as high strength, stiffness and creep resistance. CVD-SiC coatings are also constituents of the nuclear fuel particles which are considered for the fourth generation fission reactors.⁴ The CVD-SiC layer is inserted between two dense pyrocarbon layers to retain the fission products and maintain the mechanical and thermal properties of the particles under neutron irradiation at high temperature.⁴ Depending on the CVD conditions, the stoichiometry (i.e., the occurrence of free silicon or carbon phases), the crystal structure and the texture (the main orientation of the SiC crystals) in the coatings may vary, with a significant effect on the thermal and mechanical properties at room, high temperature,² and under irradiation.

Raman Microspectroscopy (RMS) is a non-destructive technique which provides information, at the micrometer scale, on the phase composition and the crystalline state (structure and texture) of materials. It is therefore particularly suited to the local analysis of

few micrometers-thick CVD coatings.³ The aim of the present paper is to investigate the structural and textural evolution of various CVD-SiC coatings, induced by room and high temperature plastic deformations and by irradiation. For this purpose, the specimens, a commercial SiC-CVD filament and a model C/SiC/C/ZrO₂ nuclear fuel particle, were submitted to (i) tensile creep at high temperature, (ii) indentation at room temperature and (iii) proton irradiation at room temperature.

2 MATERIALS AND EXPERIMENTAL PROCEDURE

6H-SiC crystals were used as a reference material for the structure and texture analyses through RMS analyses, as well as for the indentation and irradiation tests. The CVD-SiC monofilament (SCS-6) is a carbon core 140 μ m filament produced by Textron Specialty Materials. The CVD-SiC sheath is carbon rich near the carbon core and near stoichiometric (with a slight excess of free silicon) near the surface.¹⁻³ It is subsequently covered by a 3 μ m multilayer pyrocarbon (PyC) coating. The HTR (High Temperature Reactor) model nuclear fuel particle consists of a 500 μ m ZrO₂ core successively coated with a buffer porous pyrocarbon layer (95 μ m), a dense PyC inner layer (40 μ m), the 35 μ m-thick CVD-SiC layer and a dense PyC outer coating (40 μ m).

The longitudinal tensile creep testing of the monofilaments was achieved in high vacuum with a resistive heating device (isothermal gauge L₀=50mm). The load and temperature were applied during 2.2 10⁴s at 300MPa and 1400°C, respectively. To dissociate the effects of the annealing and/or the applied stress, a second non-loaded filament was simultaneously tested.

The indentation tests (MTS XP) were carried out with a diamond Berkovich tip at a maximum load of 300mN.

The proton irradiation experiments were carried out at the Phase Laboratory (Strasbourg, France). The energy, the current and the fluence were 4MeV, $0.6\mu\text{Acm}^{-2}$ and 3.10^{16}cm^{-2} , respectively.

The Raman analyses were performed with a Labram HR (Jobin Yvon) microspectrometer ($\lambda=632.8\text{nm}$, spectral resolution $\approx 2\text{cm}^{-1}$, lateral resolution $\approx 1\mu\text{m}$). A motorized micro-displacement stage ($\pm 0.1\mu\text{m}$) was used for the linescan and mapping measurements. The incident laser light propagating along the X axis of the laboratory, was plane polarised along the vertical Y axis (Tables 1-2). The back-scattered light (configuration X<Y.>-X) was analysed either without (X<Y(Y+Z)>-X) or using a rotating polariser. Two scattering arrangements were used in the later case, (i) X<YY>-X or <YY>, (polarisation of scattered light along Y) and (ii) X<YZ>-X or <YZ> (polarisation along the horizontal Z axis). The configuration <ZZ> was also examined by simply rotating the specimen of an angle $\pi/2$ and analysing the <YY> polarization.

3 RESULTS AND DISCUSSION

3-1 Raman features of SiC-based materials

SiC exists in a variety of metastable polytypes. Only one is cubic (β -SiC, zinc blende structure), the others are either hexagonal (2H (wurtzite), 4H, 6H) or rhombohedral (15R, 21R). The 3C-SiC unit cell has a T_d symmetry yielding one triply degenerate Raman active phonon (T_{2x} , T_{2y} , T_{2z}). This mode is polar and leads to an energy difference between the vibration polarised parallel to the wavevector of the phonon q (longitudinal optic: LO) and that polarised perpendicular to q (transverse optic: TO). In 3C-SiC, two Raman peaks are therefore observed corresponding to the TO and LO modes at 796cm^{-1} and 972cm^{-1} , respectively. The point group for the hexagonal polytypes is C_{6v} . It gives rise to the Raman

active A_1 , E_1 and E_2 modes. Both E_1 and E_2 are doubly degenerate (E_{1x}, E_{1y} and E_{21}, E_{22}) and only A_1 and E_1 are polar and split into TO and LO phonons.⁵ As the unit cell increases, additional phonons with different energies may appear. These new Raman bands are called folded modes, as they correspond to phonon modes located within or at the edge of the Brillouin zone.⁶ Their frequencies are obtained by folding the dispersion curves of the 3C polytype phonon modes (two optic: TO and LO and two acoustic LA and TA branches) to the centre of the Brillouin zone ($q=0$). Hence, acoustic phonons resulting from the folding of the acoustic branches are observed for the hexagonal polytypes, whereas they are forbidden for the 3C polytype.

Amorphous and/or cubic silicon, or sp^2 carbon are sometimes co-deposited in particular CVD conditions. The space group for cubic silicon is O_h and gives rise to a triply degenerate Raman active phonon ($T_{2g1}, T_{2g2}, T_{2g3}$) at 521cm^{-1} . The Si amorphous state is characterized by broad band around 480cm^{-1} . The space group corresponding to hexagonal graphite cell is D_{6h} and only phonons with the E_{2g} symmetry are Raman active. In addition to the main E_{2g} mode (referred to as the G band at $\approx 1580\text{cm}^{-1}$), the spectra of sp^2 carbons generally exhibit features assigned to structural disorder (e.g., the D and D' bands around 1335 and 1615cm^{-1} , respectively). Their intensity and width both increase with the amount of disorder.⁷

Except $E_1(\text{LO})$ (which is not observable in the back-scattering geometry), all the optical phonons characteristic of the 6H-SiC phase ($E_{2(\text{low})}=767\text{cm}^{-1}$, $E_{2(\text{high})}=789\text{cm}^{-1}$, $E_1(\text{TO})=798\text{cm}^{-1}$ and $A_1(\text{LO})=966\text{cm}^{-1}$) are clearly identified on the Raman spectra recorded for various polarisations and orientations of the SiC single crystal (Fig. 1). Besides these strong optical modes, a weak additional $A_1(\text{LO})$ peak is observed at 889cm^{-1} , together with several acoustic features ($E_1(\text{TA})=240\text{cm}^{-1}$, $E_2=266\text{cm}^{-1}$, $A_1(\text{LA})$ doublet at 505 and 514cm^{-1}).

The cross section of the SCS-6 filament has been examined by RMS. The Raman analyses confirm the dual structure of the CVD-SiC sheath, consisting of a carbon rich SiC

layer near the carbon core (as shown by the presence of the D and G bands) and a near stoichiometric SiC outer layer (Fig. 1).¹⁻³ The broad carbon features correspond to a very disordered form (turbostratic, with heavily distorted graphene layers). The various optical modes evidenced for the 6H-SiC crystal are also present for the outer CVD-SiC. The Raman peaks appear at similar frequencies but with larger widths and overlapping, due to a lower crystalline state. Very large bands below 600cm^{-1} (due to acoustic phonons) and at $600\text{-}1000\text{cm}^{-1}$ (characteristic of a density of state) are also observed. These broad bands are likely due to the scattering of sub-micron size crystals and/or grain boundaries. The occurrence of multiple overlapping modes in the TO region ($750\text{-}810\text{ cm}^{-1}$) does not support the existence of pure cubic or hexagonal polytypes. These features are rather characteristic of a coherent structure involving a high density of stacking faults along the [111]-cubic or [001]-hexagonal direction (i.e., along the compact Si-C planes direction).

The Raman spectra from the cross section of the SiC-CVD sheath of the HTR particle show mainly two sharp peaks at 796 and 772cm^{-1} , typical of the 3C polytype and a very weak component at 767cm^{-1} , probably due to a low proportion of stacking faults (Fig. 1). No evidence of any secondary phase could be shown.

3-2 Influence of the crystal orientation on the phonon intensities

The intensities of the various phonons vary with the orientation of the crystal (xyz) about the laboratory axes (XYZ). The scattering efficiency (I) is related to the polarization of the incident (e_i) and scattered (e_s) light and is given by $I=C\sum_j |e_i \cdot R(j) \cdot \xi_j \cdot e_s|^2$, where C is a constant, R_j is the Raman tensor and ξ_j is the polarization of the phonon j.⁸ The expressions of the Raman tensors were given by Loudon for the various crystal symmetry classes.⁸ For both T_d and O_h , the crystal coordinate system (x, y, z) is chosen along the [100], [010] and [001] crystal axes, whereas for C_{6v} , the z axis is taken as the c [001] direction and the x and y axes

are perpendicular to z and to one another. For the D_{6h} symmetry, the tensors for the non polar Raman active E_{2g1} and E_{2g2} modes are respectively equivalent to the $E_{2(1)}$ and $E_{2(2)}$ above expressions. The T_2 , A_1 and E_1 modes are polar. The intensities of the LO and TO vibrations therefore vary with the propagation directions in the crystal (Table 1-2). In the back-scattering configuration, q is parallel to the light propagation, i.e., to the X axis of the laboratory. The consequence is straightforward for both the A_1 and E_1 modes, as $A_1(\text{LO})$ is active when q is along the c axis of the crystal, whereas the $A_1(\text{TO})$ and $E_1(\text{TO})$ modes are active when q is perpendicular to c . For the cubic zinc-blend crystal, the assessment of the TO and LO peak intensities is more complex. It can be shown, for instance, that the TO mode is strictly forbidden for the $[100]$ crystal orientation, whereas the LO mode is forbidden for the $[110]$ orientation. The calculated phonon intensities as a function of the scattering geometry and the main crystal orientation is given in Table 1-2. The intensity factors of the TO-LO components have been marked out (e.g., e and e') due to the different electro-optic coefficients.⁹

The selection rules of the various TO and LO-region phonons, for the cubic and the hexagonal SiC polytypes, show only few common features when considering the orientation of the compact Si-C plane axes with respect to the X axis. For instance, the influence of the polarization configuration and the rotation angle of the crystal about the X axis is similar when examining (i) respectively the $T_2(\text{TO})$ and the $T_2(\text{LO})$ modes, for the cubic- $[111]$ crystal orientation and (ii) the E_2 and the $A_1(\text{LO})$ modes, for the hexagonal- $[001]$ direction (Table 1-2). Conversely, if the dense Si-C plane axis is perpendicular to the X axis (i.e., when analysing the $[112]$ -cubic and $[100]$ -hexagonal crystal face respectively), the $A_1(\text{LO})$ mode is forbidden for all polarizations, whereas the $T_2(\text{LO})$ mode appears in certain polarization conditions.

Raman spectra were recorded from the 6H-SiC crystal with different orientations. All the optical modes and most of the acoustic features are well identified and obey strictly the above

selection rules (Table 1). The high intensity peak at 789cm^{-1} was shown to be a superposition of two phonons with $A_1(\text{TO})$ and E_2 symmetries.⁵ The measured intensities were used to determine the characteristics of the analyzer (efficiency, transmittance) and the parameters a, b, c and d of the Raman matrices. RMS measurements were also performed as a function of the rotation angle θ of the 6H-SiC crystal about the X axis (laser axis), with X either parallel or perpendicular to the c [001] axis.¹⁰ Intensity predictions were also made for both cubic and hexagonal systems. When the [111]-c or the [100]-h axes are parallel to the X axis, the intensities of the $T_2(\text{TO})$ and $T_2(\text{LO})$ modes, and the $A_1(\text{LO})$ and E_2 modes respectively, remain constant whatever θ . Conversely, when the [111]-cubic or [100]-hexagonal axes are perpendicular to X, the intensities of the $T_2(\text{TO})$, $T_2(\text{LO})$, $A_1(\text{TO})$, $E_1(\text{TO})$ and E_2 modes vary significantly with θ and follow sinusoidal laws of periods π or $\pi/2$. The experimental data obtained from the 6H-SiC crystal were found to match the calculated intensities very accurately. This approach was used to analyze the texture of the various CVD-SiC coatings.

3-3 Structure and texture analysis of the as-processed materials

The cross sections of both the as-processed SCS-6 filament and the HTR fuel particle were submitted to RMS mappings. RMS mappings with the two scattering configurations ($X\langle YY\rangle-X$ and $X\langle YZ\rangle-X$) were recorded to examine the effect of the coating orientation on the phonon intensities, to evidence any preferential orientation of the crystallites. The intensity of the various modes was computed for all spectra along the cross-section and plotted as phonon intensity, bandwidth (FWHM) or frequency linescans or mappings (figure 2-3).

The HTR particle is fully stoichiometric throughout the whole section whereas the dual inner carbon rich/outer stoichiometric structure of the CVD-SiC filament appears clearly on the Raman intensity mappings for the SiC and carbon features (Fig. 2-3). The cross sections

of the filament and the HTR particle are both circular. The punctual analysis of the SiC coating as a function of the rotation angle θ about the X axis is therefore equivalent to the tangential scanning analysis of the coating. The anisotropy of the SiC-CVD coatings of the SCS-6 filament is clearly noticeable from the symmetrical SiC features intensity patterns. The mappings show either two or four center-symmetrical minima/maxima spots, the geometry of which is characteristic of the phonon symmetry (Fig. 3). These features are explicitly related to the periodic intensity functions (of periods π or $\pi/2$) established above for the SiC crystal as a function of the rotation angle θ about X, when the [111]-c or [100]-h direction is perpendicular to X. The preferential orientation of the dense Si-C planes normal to the CVD growth direction is clearly established. The cubic or hexagonal selection rules are obviously not strictly obeyed, due to the faulted SiC structure and the angular dispersion of the crystals in the coating. However, such a coherent SiC structure containing random or periodic stacking faults along a single anisotropy direction, gives rise to phonon symmetries closer to those of the 6H-structure than 3C. This is confirmed for instance by the absence of the LO feature on the spectra from the transverse filament cross section whereas it is observed from a longitudinal cross section.

The TO and LO mappings of the HTR particle show contrasted domains of a few micrometers (i.e., larger than the spatial resolution) related to β -SiC crystals with different orientations. The peripheral scan along the coating did not reveal any variation of the average intensity values, suggesting that the polycrystalline β -SiC coating is isotropic. The absence of texturing was indeed confirmed by TEM analyses, although a slight preferential orientation was observed by electron back scattering diffraction.

3-4 RMS analysis of the crept SCS-6 filament

Both the annealed ($T=1400^{\circ}\text{C}$, $t=2.2 \cdot 10^4\text{s}$, $\sigma=0\text{MPa}$) and crept ($T=1400^{\circ}\text{C}$, $t=2.2 \cdot 10^4\text{s}$, $\sigma=300\text{MPa}$) SCS-6 filaments were submitted to RMS analyses and compared to the as-processed specimens. The RMS analyses did not evidence any change in the radial distribution of the SiC and free carbon phases. However, the near stoichiometric outer region of both the annealed and crept specimens showed the presence of a sharp peak at 524cm^{-1} , indicative of the presence of crystallized free silicon (Fig. 4). The cubic silicon phase segregates and crystallizes from the initial amorphous intergranular phase which is co-deposited by CVD (at about 1100°C). The relatively high frequency of the silicon peak (521cm^{-1} expected in cubic Si) denotes a significant compressive stress state, likely due the SiC/Si thermal expansion mismatch.

In order to assess the structural changes induced by the annealing/creep tests, the bandwidths of the various characteristic peaks were examined through the diameter of the filaments (Fig. 2). The bandwidth (FWHM) is indeed directly related to the crystal size for both silicon and SiC. The FWHM values of both the G and D bands also vary significantly with the structure of pyrocarbons. They are rather related, in this case, to the in-plane local defects or wrinkled graphene layers.

The presence of co-deposited free carbon in the inner region of the as-processed filament is associated to a smaller SiC grain size (or a larger bandwidth) than in the near stoichiometric outer region (Fig. 2). The same holds true for the annealed and crept specimens. However, a significant increase of the grain size is observed after both annealing and creep (20% decrease of FWHM), indicating a predominant influence of the temperature with respect to stress. A much more considerable decrease of the FWHM value of the D band is observed after annealing and creep (of about 50%), which is associated to a significant ordering of the graphene layers (Fig. 2). A slight effect of the stress is also discernible. It is generally admitted that within the present temperature range, the creep deformation of CVD-SiC occurs

through a SiC grain boundary (GB) sliding/locking mechanism, accommodated by GB diffusion.¹¹⁻¹² The intergranular free carbon phase, present in the inner part of the filament, hinders the grain sliding and therefore improves significantly the creep resistance of CVD-SiC.¹² However, the free carbon phase is likely submitted to shear strains due to the GB sliding, which promote the basal plane alignment and ordering, as suggested by RMS. Although the presence of free silicon at GB accelerates drastically creep ($T_f=1410^\circ\text{C}$),¹¹, the segregation and the crystallization of silicon evidenced by RMS are essentially controlled by diffusion. They are therefore merely activated by temperature (no effect of stress was observed by RMS).

The specimens were also submitted to RMS mappings, to investigate the texture changes of the various phases (Fig. 3). In association with the limited SiC grain growth, no significant change of the preferential orientation of the SiC crystals was observed after both annealing and creep (the Si-C planes retaining their marked radial orientation). Whereas the silicon grains showed a random orientation, a texturing of the graphene layers was induced slightly by annealing and more significantly by creep (Fig. 3). The two-polarization intensity patterns account for a radial texturing, i.e., a preferential orientation of the basal planes parallel to the growth direction. This very unusual texture (in pyrocarbons, basal planes are mostly oriented perpendicular to the growth direction or parallel to the substrate) is very likely related to the radial and columnar structure of the SiC phase. The slight SiC grain restructuring, and the more effective grain sliding accommodated creep, indeed both induce a flattening of the intergranular graphene layers, resulting in such a particular radial carbon texturing.

3-5 RMS analysis of the indented 6H-SiC crystal and HTR particle

Both the [001] and [100] 6H-SiC crystal faces as well as the cross section of the CVD-SiC layer of the HTR particle (HTR-SiC) were indented and examined by RMS. All the

specimens showed elastoplastic behaviours and relatively similar properties. Identical pyramidal indenter prints due to plastic deformations were found for all the as-indented specimens. Radial cracks were also usually found at the angles of the print.

The local RMS analyses of the indented zone revealed a strong decrease of the intensity and a broadening of all the initial sharp acoustic (for the 6H-SiC only) and optic phonons (for both 6H-SiC and HTR-SiC), obviously related to some structural damages (Fig. 5-7,9). These damages are highly concentrated in the plastic region. However, particularly in the case of the 6H-SiC, they also extend beyond this zone in particular directions, not necessarily related to the indenter edges (Fig. 6-7). Broad acoustic features (below 500cm^{-1} , around 600cm^{-1} and within the optical phonon $700\text{-}1000\text{cm}^{-1}$ region) appear simultaneously, which are strictly limited to the plastic strained region. This is for instance illustrated on Figure 7 showing the $A_1(\text{LO})$ -intensity and bandwidth mappings as well as the broad 600cm^{-1} acoustic mode intensity pattern recorded from the [001] face (configuration $\langle\text{YY}\rangle$ or $z\langle\text{xx}\rangle-z$). Particular intensity and FWHM patterns are also observed for the $E_1(\text{TO})$ mode, from the [001] face, in the configuration $\langle\text{YZ}\rangle$ (or $x\langle\text{zy}\rangle-x$). These patterns clearly show a narrow damaged line along the Y axis, probably due to a radial crack, as well as a horizontal broad damaged zone extending along the Z axis (along the [001] planes) (Fig. 6). The broad acoustic modes are common to the plastic regions of both 6H-SiC and HTR-SiC and are non-polarized modes (Fig. 7,9).

In order to reveal the structural disorders responsible for the various Raman feature changes, a slight chemical etching (in boiling Murakami reagent) of the indented specimens was carried out before SEM observations. The initial smooth plastic print region was first removed during etching, revealing the defects extending underneath (Fig. 8,10). The etched [100] 6H-SiC specimen clearly showed a layered structure parallel to the [001] planes, with extensive layer distortion and cleavage under the indenter (Fig. 8a). This morphology is likely

related to dislocation nucleation and slip, as a consequence of the plasticity response of 6H-SiC to indentation.¹³ It can be obviously associated to the diffuse damaged zone on the $E_1(\text{TO})/\langle \text{YZ} \rangle$ intensity pattern, spreading along the same [001] direction (Fig. 6). The etched [001] 6H-SiC specimen showed a complex layered structure, with three distinct directions at the edges of the print (forming a $2\pi/3$ angle respectively) and interconnecting at the centre of the print (Fig. 8b). This morphology is probably related to the dislocation loop rosettes observed by Page et al. by TEM.¹³ The dislocation loops were usually found to extend in three preferential crystallographic directions, possibly due to different shear stress components on distinct crystallographic orientations. As a consequence, the main axes of the damaged zone (i.e., with a high density of loop dislocation) evidenced on the Raman intensity pattern, do not coincide with those of the print edges (Fig. 7). A strong intensity decrease of the broad acoustic bands was observed after etching. These features were therefore attributed to the most severe structural disorders induced immediately under the indenter tip and eliminated by etching. These defects are likely diverse, e.g., high densities of dislocations, stacking faults and possibly also boundaries or free surfaces of twisted small grains appearing along the indentation edges.¹⁴

The etched HTR-SiC specimen reveals the polycrystalline structure of the specimen, with interlocked microcrystals having random orientations (Fig. 10). The main defects induced by indentation appear as cleavage, with parallel layers running through crystals having appropriate orientations (the layers direction being close to those of the print boundaries). As for 6H-SiC, the dislocation nucleation and motion occurring in crystals close to the indentation, are likely responsible for such a morphology and the structural changes evidenced by RMS (i.e., intensity decrease and broadening of the TO and LO peaks) (Fig. 9). The irregular shape of the Raman intensity and FWHM pattern is due to the isotropic microcrystalline nature of the HTR-SiC, the various orientations of the crystals giving rise to

locally different structural alterations. Conversely, the most severe structural disorders, as evidenced by the broad acoustic bands, were only observed very locally under the indenter tip (Fig. 9d).

3-6 RMS analysis of the irradiated 6H-SiC crystal and HTR particle

Only the parts of the specimens exposed to the source of ions were examined. These zones were easily identified from their darkening, a phenomenon strongly suggesting the occurrence of punctual defects. All the original acoustic and optic Raman features were found unaltered (no change in intensity and FWHM) after irradiation for both materials and in all scattering configurations (Fig. 11). However, new weak, but well defined bands were observed at 570-630 cm^{-1} (very similar to that found after indentation), 830-850 cm^{-1} (relatively sharp and asymmetrical) and 820-970 cm^{-1} (very broad, lying between the main TO and LO peaks). These modes are not polarized (Fig. 11).

The space localisation of phonon (e.g., due to nanocrystals or to lattice imperfections) generally results in broadened, asymmetrical and lower frequency bands.^{3,15-16} In order to investigate the disorder ranges induced by irradiation, a phonon confinement model was applied to 3C-SiC to simulate the Raman spectra.^{3,15-16} The intensities $I_i(\omega)$ of the various phonons i were integrated along all the acoustic (TA, LA) and optic (TO, LO) branches $\omega_i(q)$, within the Brillouin zone ($0 \leq q \leq 1$), using the weighing function $f(q, L) = \exp(-q^2 L^2 / 4)$, centred on $q=0$, where q is the reduced wave vector, L is a dimensionless parameter ($L=1$ correspond to the nearest-neighbour Si (or C) planes) and Γ_{0i} are the linewidths of the undistorted Raman lines (all arbitrary fixed at $\Gamma_{0i}=10\text{cm}^{-1}$, equation (1)).

$$I_i(\omega) = \int_0^1 \frac{f(q, L)^2}{(\omega - \omega_i(q))^2 + \Gamma_{0i}^2 / 4} d^3 q \quad (1)$$

An example of calculated spectrum ($\Gamma_{0i}=10\text{cm}^{-1}$, $L=2$) is shown in Figure 12. The model gives a relatively accurate description of the experimental spectrum. It accounts in particular for the broadening of the TO and LO phonons, their asymmetrical shape (e.g., the low frequency tail of the LO phonon), the broad 600cm^{-1} acoustic band (as a consequence of the LA density of state), as well as the wide $820\text{-}970\text{cm}^{-1}$ band and the new asymmetrical 840cm^{-1} feature due respectively to the density of state and the $q=1$ edge of the LO branch (Fig. 12). The influence of the parameter Γ_{0i} is essentially to modify the bandwidth of all the optical and acoustic features. It is worthy of note that an increase of L ($L>3$), while gradually delocalizing the LO phonon, results in the vanishing of the 840cm^{-1} component. The presence of such a low-scale disorder-induced experimental feature supports the occurrence of punctual defects. A similar irradiation-induced low frequency component of the TO phonon is not clearly evidenced on the experimental spectra, as they already display folded modes due either to polytypism (seen as intense discrete modes), for 6H-SiC, or few stacking faults (visible as weak and broad shouldering), for HTR-SiC.

4 CONCLUSION

SiC based CVD coatings of two different natures have been examined by RMS, to characterize precisely their phase composition, structure and microtexture, in their as-processed state and after different tests, i.e., high temperature annealing and creep, indentation and irradiation at room temperature.

Depending on the processing conditions, the CVD coatings were found either stoichiometric, or free silicon (or carbon) rich. The SiC crystallites were predominantly cubic with variable amounts of stacking faults along the [111] axis. The large interlocked β -SiC

crystallites of HTR-SiC form an isotropic texture whereas the submicrometric and faulted crystallites of the SCS-6 filament give rise to a preferential orientation of their single stacking faults axis parallel to CVD-growth.

Both annealing and creep (in the same temperature and time conditions) resulted in the same degree of crystal growth and decrease of stacking faults. A slight stress influence was however observed on the structure and texture of the co-deposited free-carbon, likely as a consequence of the intergranular creep mechanism.

Room temperature indentation induces severe structural disorders (dislocations, stacking faults, fragmentation of grains) immediately under the indenter and more extended damages due to dislocation slip parallel to the compact Si-C planes. The structural changes induced by indentation and revealed by RMS depend on the crystal orientation and therefore on the texture of polycrystalline SiC.

The irradiation of the specimens by protons at room temperature produced only small amounts of disorders. The specific alterations of the Raman features were explained using a phonon confinement model. The value of the best-fit localization parameter accounts for very low scale defects, likely as punctual defects.

ACKNOWLEDGMENTS

The authors are indebted to J.J. Grob from the PHASE Laboratory, for performing the proton irradiation. They greatly acknowledge C. Sauder and O. Dugne for valuable discussions as well as Framatome ANP (an AREVA and Siemens Company), for the financial support of the R&D on the HTR fuel.

REFERENCES

1. Ning, X.J. and Pirouz, P., The microstructure of SCS-6 SiC fiber, *J. Mater. Res.*, 1991, **6**(10), 2234-2248.
2. Chollon, G. and Naslain, R., Chemical and Thermo-mechanical properties of SiC-based reinforcements, *Ceram. Eng. Sci. Proc.*, 2000, **21**(4), 339-345.
3. Ward, Y., Young, R.J. and Shatwell, R.A., A Microstructural study of silicon carbide fibres through the use of Raman microscopy, *J. Mater. Sci.*, 2001, **36**, 55-66.
4. Charollais, F., Fonquernie, S., Perrais, C., Perez, M., Cellier, F. and Vitali, M.P., CEA and AREVA R&D on V/HTR Fuel Fabrication with the CAPRI Experimental Manufacturing Line. In the Proceedings of the 2005 European Nuclear Conference (Versailles, France, December 11-14th, 2005), CD-ROM, 2005.
5. Feldman, D.W., Parker Jr, J.H., Choyke, W.J. and Patrick, L., Phonon Dispersion Curves by Raman Scattering in SiC Polytypes 3C, 4H, 6H, 15R and 21R, *Phys. Rev.*, 1968, **173**(3), 787-793.
6. Nakashima, S., Katahama, H., Nakakura, Y. and Mitsuishi, A., Relative Raman intensities of the folded modes in SiC polytypes, *Phys. Rev. B*, 1986, **33**(8), 5721-5729.
7. Cuesta, A., Dahmelincourt, P., Laureyns, J., Martinez-Alonzo, A. and Tarascon, J.M.D., Raman microprobe study on carbon materials, *Carbon*, **32**(8), 1994, 1523-1532.
8. Loudon, R. , The Raman effect of crystals, *Adv. Phys.*, 1964, **13**, 423-482.
9. Arguello, C.A., Rousseau, D.L. and Porto, S.P.S , First-order Raman effect in Wurtzite-type crystals, *Phys. Rev.*, 1969, **181**(3), 1351-1363.
10. Chollon, G., Vallerot, J.M., Grente, K., Shatwell, R.A. and Couzi, M., Local texture analyses of ceramic and carbon composites through Raman microspectroscopy mappings. In *High Temperature Ceramic Matrix Composites 5*, ed. M. Singh, R.J. Kerans, E. Lara-

- Cursio and R. Naslain. The American Ceramic Society, Westerville-Ohio, 2005, pp. 557-562.
11. Di Carlo, J.A., Creep of chemically vapour deposited SiC fibres, *J. of Mater. Sci.*, 1986, **21**, 217-224.
 12. Lewinson, C.A., Giannuzzi, L.A., Bakis, C.E. and Tressler, R.E., High temperature creep and thermostructural evolution of chemically vapor-deposited silicon carbide, *J. Am. Ceram. Soc.*, 1999, **82**(2), 407-413.
 13. Page, T.F., Riester, L. and Hainsworth, S.V., The plasticity response of 6H-SiC and related isostructural materials to nanoindentation: slip vs densification, *Mat. Res. Soc. Symp. Proc.*, 1998, **522**, 113-118.
 14. Yang, J.W. and Pirouz, P., The $\alpha \rightarrow \beta$ polytypic transformation in high temperature indented SiC, *J. Mater. Res.*, 1993, **8**(11), 2902-2907.
 15. Richter, H., Wang, Z.P. and Ley, L., The one phonon Raman spectrum in microcrystalline silicon, *Solid. State Commun.*, 1981, **39**, 625-629.
 16. Rohmfeld, S., Hundhausen, M. and Ley, L., Raman scattering in polycrystalline 3C-SiC: influence of stacking faults, *Phys. Rev. B*, 1998, **58**(15), 9858-9862.

FIGURE CAPTIONS

- Figure 1: Raman spectra of the various SiC-based materials
- Figure 2: FWHM profiles across the SCS-6 filaments (a) D band, (b) SiC-TO peak
- Figure 3: Intensity mappings of the SCS-6 filaments (a) optical micrograph, (b)-(c) SiC-TO peak, as-processed filament, (d)-(e) D band, crept filament
- Figure 4: Raman spectra from the crept SCS-6 filament (a) near stoichiometric outer CVD-SiC, (b) carbon-rich inner CVD-SiC (spectra (1)-(4) from positions shown in Fig 3a)
- Figure 5: Raman spectra from the pristine and indented specimens (a) 6H-SiC, (b) HTR-SiC
- Figure 6: Intensity and FWHM mappings of indented 6H-SiC ([001] face) (a) optical micrograph, (b) I-E₁(TO), (c) FWHM-E₁(TO)
- Figure 7: Intensity and FWHM mappings of indented 6H-SiC ([100] face) (a) optical micrograph, (b) I-A₁(LO), (c) FWHM-A₁(LO), (d) I-Ac(600cm⁻¹) mode
- Figure 8: SEM micrograph of indented and etched 6H-SiC (a) [100] face, (b) [001] face
- Figure 9: Intensity and FWHM mappings of indented HTR-SiC (a) optical micrograph, (b) I-LO, (c) FWHM-LO, (d) I-Ac(600cm⁻¹) mode
- Figure 10: SEM micrograph of indented and etched HTR-SiC
- Figure 11: Raman spectra from the irradiated specimens (a) 6H-SiC, (b) HTR-SiC
- Figure 12: Spectrum of disordered SiC, as simulated by a spatial correlation model

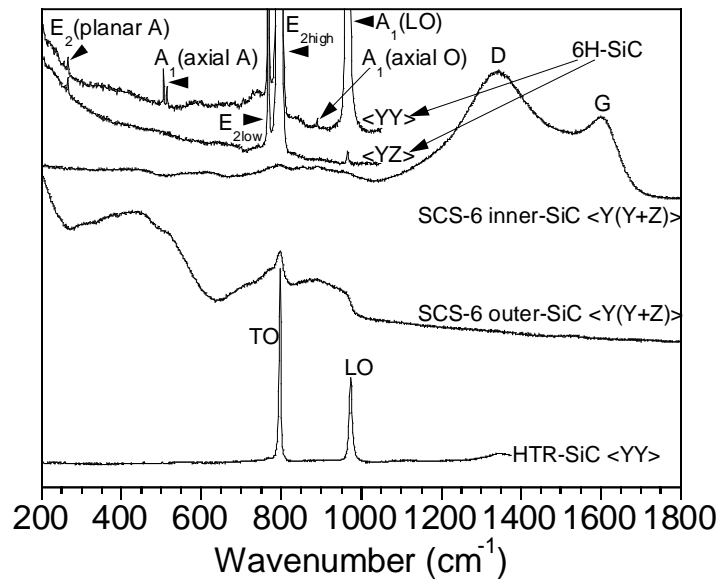


Figure 1: Raman spectra of the various SiC-based materials

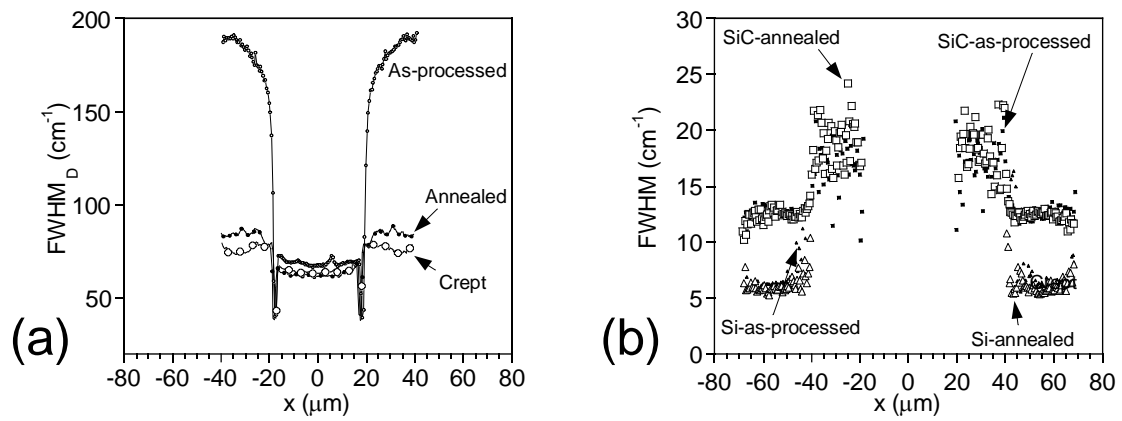


Figure 2: FWHM profiles across the SCS-6 filaments (a) D band, (b) SiC-TO peak

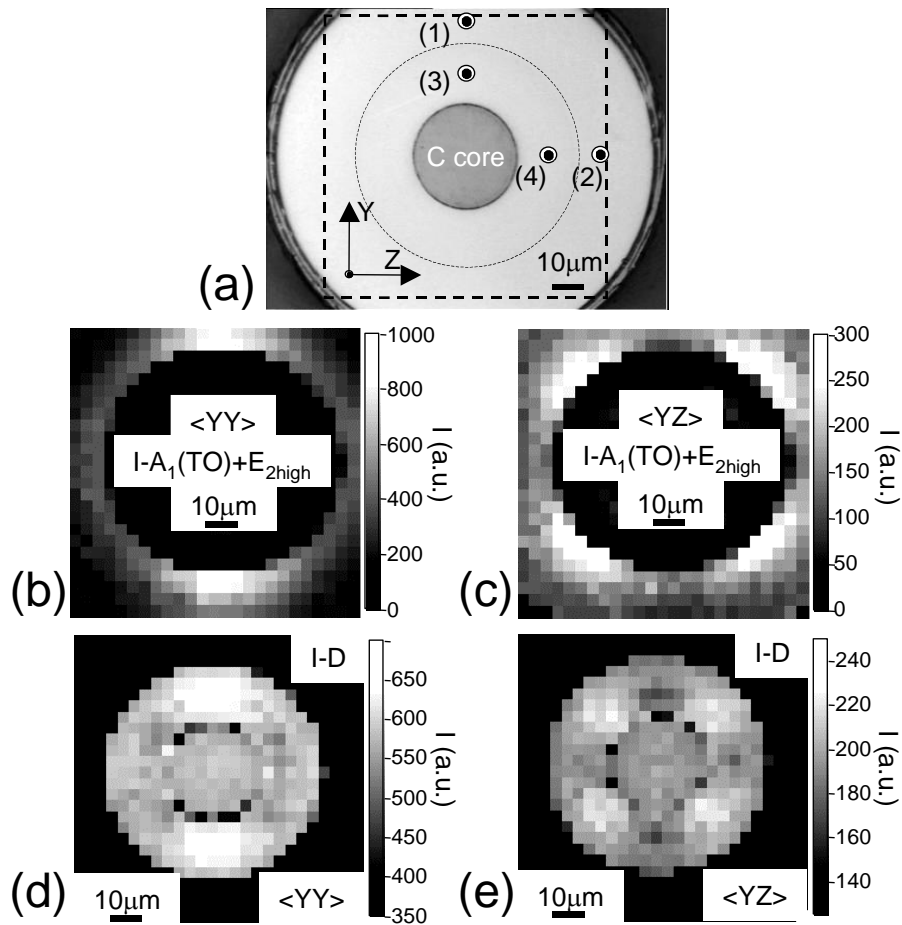


Figure 3: Intensity mappings of the SCS-6 filaments (a) optical micrograph, (b)-(c) SiC-TO peak, as-processed filament, (d)-(e) D band, crept filament

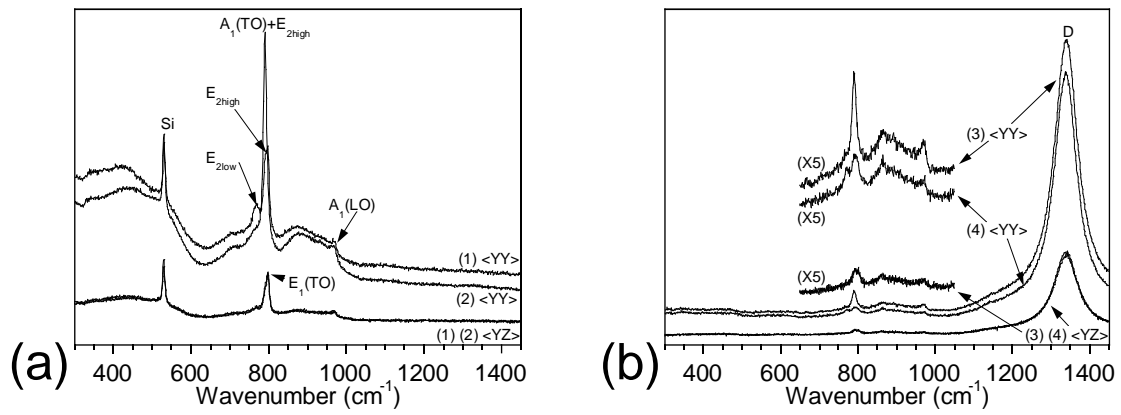


Figure 4: Raman spectra from the crept SCS-6 filament (a) near stoichiometric outer CVD-SiC,

(b) carbon-rich inner CVD-SiC (spectra (1)-(4) from positions shown in Fig 3a)

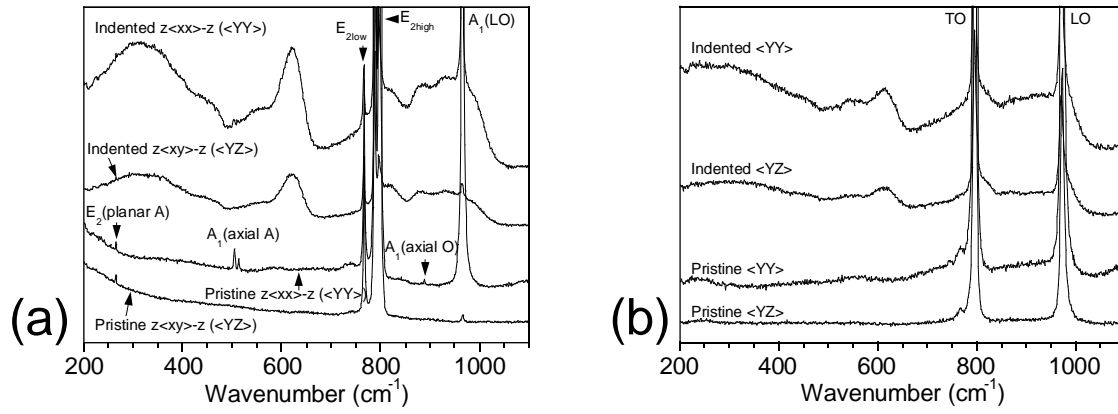


Figure 5: Raman spectra from the pristine and indented specimens (a) 6H-SiC, (b) HTR-SiC

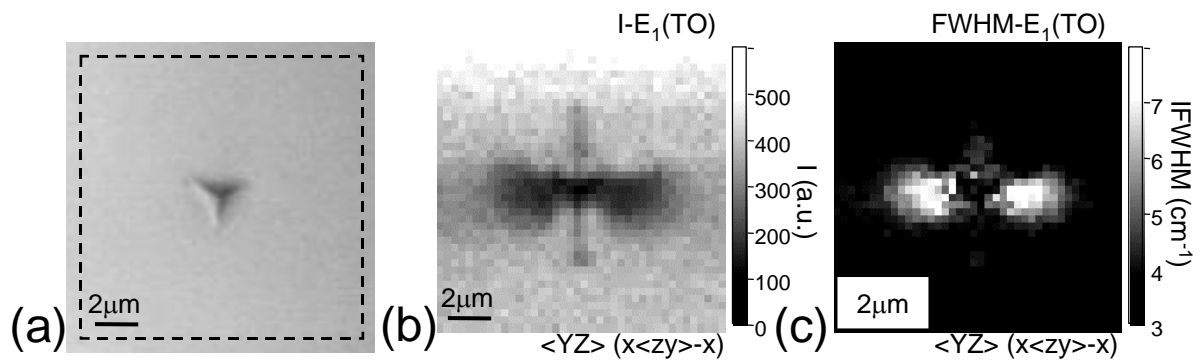


Figure 6: Intensity and FWHM mappings of indented 6H-SiC ([001] face) (a) optical micrograph,

(b) $I-E_1(\text{TO})$, (c) $\text{FWHM}-E_1(\text{TO})$

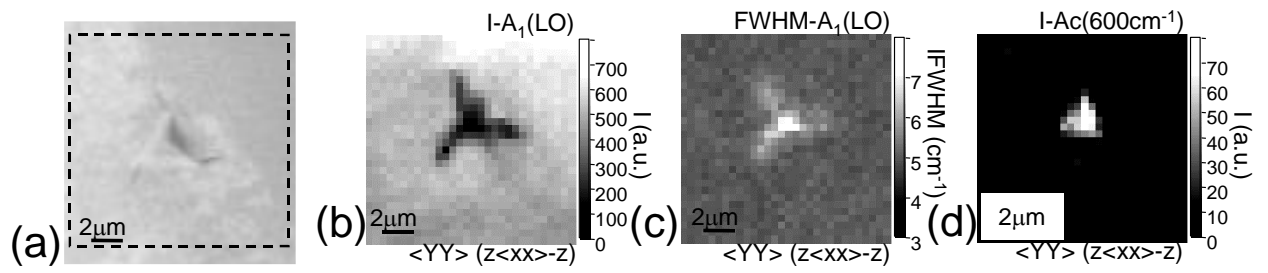


Figure 7: Intensity and FWHM mappings of indented 6H-SiC ([100] face) (a) optical micrograph,

(b) I-A₁(LO), (c) FWHM-A₁(LO), (d) I-Ac(600cm⁻¹) mode

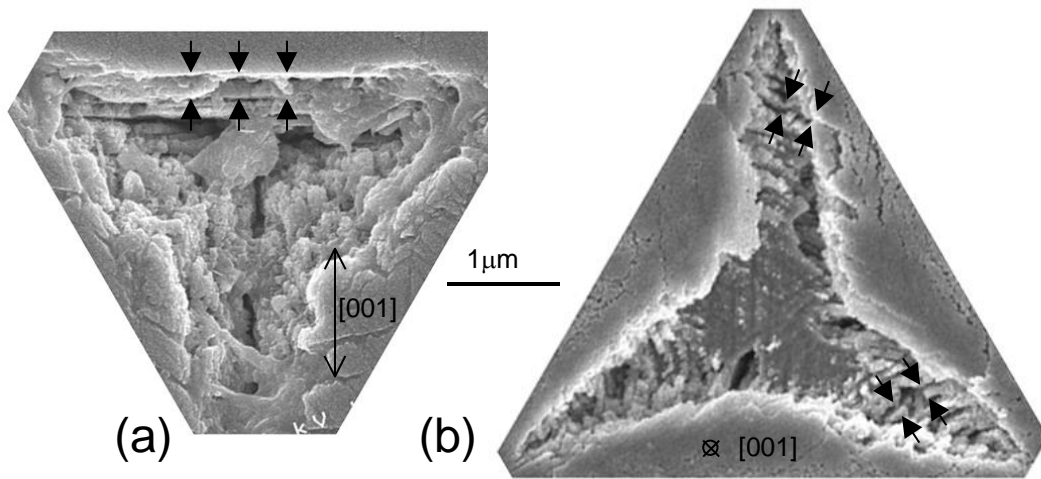


Figure 8: SEM micrograph of indented and etched 6H-SiC (a) [100] face, (b) [001] face

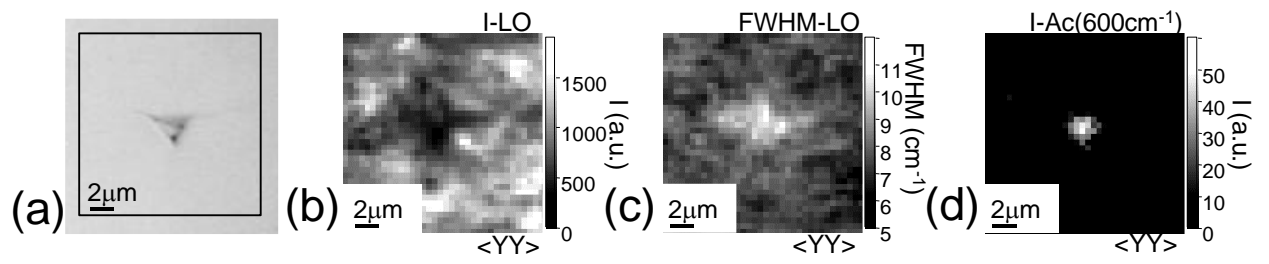


Figure 9: Intensity and FWHM mappings of indented HTR-SiC (a) optical micrograph,

(b) I-LO, (c) FWHM-LO, (d) I-Ac(600cm^{-1}) mode

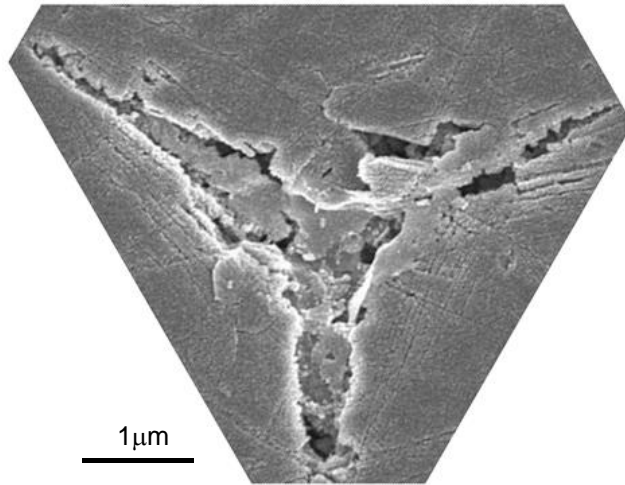


Figure 10: SEM micrograph of indented and etched HTR-SiC

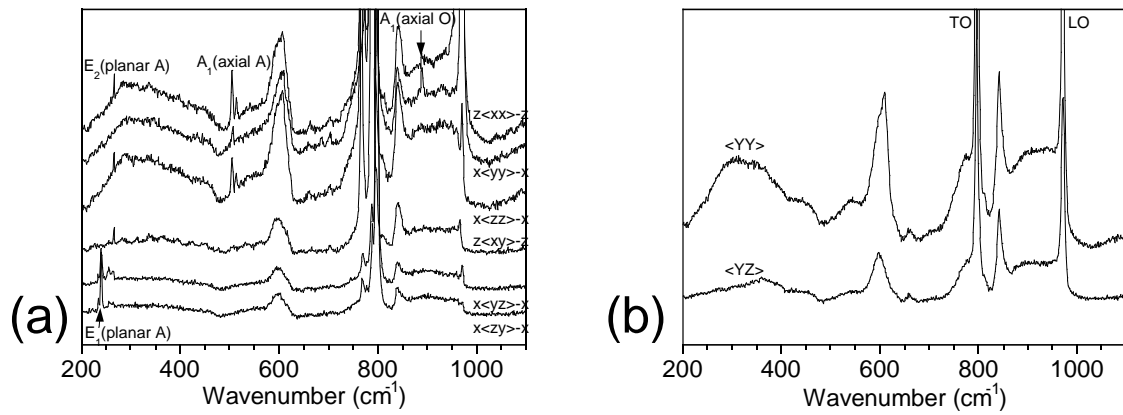


Figure 11: Raman spectra from the irradiated specimens (a) 6H-SiC, (b) HTR-SiC

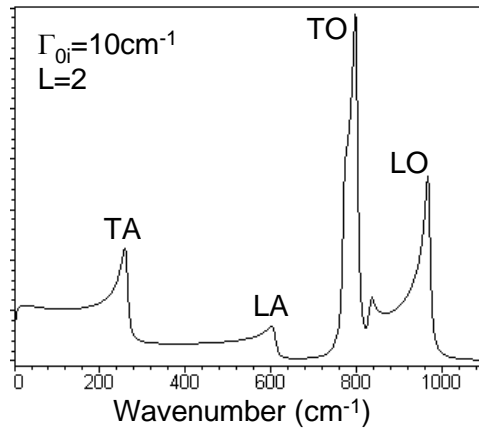


Figure 12: Spectrum of disordered SiC, as simulated by a spatial correlation model

TABLE CAPTIONS

Table1: Phonon intensities as a function of the scattering geometry (T_d symmetry)

Table2: Phonon intensities as a function of the scattering geometry (C_{6v} symmetry)

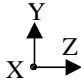
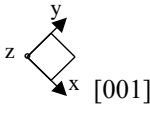
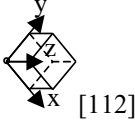
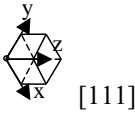
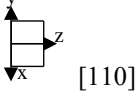
T_d	$T_2(TO)$			$T_2(LO)$		
	$\langle YY \rangle$	$\langle YZ \rangle$	$\langle ZZ \rangle$	$\langle YY \rangle$	$\langle YZ \rangle$	$\langle ZZ \rangle$
 [001]	0	0	0	e^2	0	e^2
 [112]	$1/3e^2$	$1/3e^2$	$4/3e^2$	$2/3e^2$	0	0
 [111]	$2/3e^2$	$2/3e^2$	$2/3e^2$	$1/3e^2$	0	$1/3e^2$
 [110]	e^2	e^2	0	0	0	0

Table1: Phonon intensities as a function of the scattering geometry (T_d symmetry)

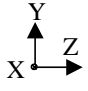
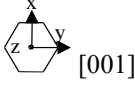
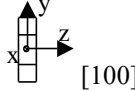
C_{6v}	$A_1(\text{TO})$			$A_1(\text{LO})$			$E_1(\text{TO})$			E_2		
	YY	YZ	ZZ	YY	YZ	ZZ	YY	YZ	ZZ	YY	YZ	ZZ
 [001]	0	0	0	a^2	0	a^2	0	0	0	d^2	d^2	d^2
 [100]	a^2	0	b^2	0	0	0	0	c^2	0	d^2	0	0

Table2: Phonon intensities as a function of the scattering geometry (C_{6v} symmetry)